The Astrophysical Journal, 941:134 (14pp), 2022 December 20 https://doi.org/10.3847/1538-4357/ac9ea4

Evaluating Lyα Emission as a Tracer of the Largest Cosmic Structure at $z \sim 2.47$

Yun Huang[1,14], Kyoung-Soo Lee[1,14], Olga Cucciati[2], Brian C. Lemaux[3], Marcin Sawicki[4], Nicola Malavasi[5,14], Vandana Ramakrishnan[1,14], Rui Xue[6,14], Letizia P. Cassara[7], Yi-Kuan Chiang[8], Arjun Dey[9], Stephen D. J. Gwyn[10], Nimish Hathi[11], Laura Pentericci[12], Moire K. M. Prescott[13], and Gianni Zamorani[2]
[1] Department of Physics and Astronomy, Purdue University, 525 Northwestern Avenue, West Lafayette, IN 47907, USA
[2] INAF-Osservatorio di Astrofisica e Scienza dello Spazio di Bologna, Via Piero Gobetti 93/3, I-40129, Bologna, Italy
[3] Gemini Observatory, NSF's NOIRLab, 670 N. A'ohoku Place, Hilo, Hawai'i, 96720, USA
[4] Institute for Computational Astrophysics and Department of Astronomy & Physics, Saint Marys University, 923 Robie Street, Halifax, NS B3H 3C3, Canada
[5] Université Paris-Saclay, CNRS, Institut d'Astrophysique Spatiale, F-91405, Orsay, France
[6] National Radio Astronomy Observatory, 520 Edgemont Road, Charlottesville, VA 22903, USA
[7] INAF-IASF Milano, via Alfonso Corti 12, I-20129 Milano, Italy
[8] Institute of Astronomy and Astrophysics, Academia Sinica, Taipei 10617, Taiwan
[9] NSF's National Optical-Infrared Astronomy Research Laboratory, 950 N. Cherry Ave., Tucson, AZ 85719, USA
[10] Herzberg Astronomy and Astrophysics Research Centre, National Research Council, 5071 W. Saanich Rd. Victoria, BC, V9E 2E7, Canada
[11] Space Telescope Science Institute, Baltimore, MD, USA
[12] INAF, Osservatorio Astronomico di Roma, via Frascati 33, I-00078 Monteporzio Catone, Italy
[13] Department of Astronomy, New Mexico State University, P.O. Box 30001, MSC 4500, Las Cruces, NM 88033, USA
Received 2022 June 14; revised 2022 October 18; accepted 2022 October 28; published 2022 December 16

Abstract

The discovery and spectroscopic confirmation of Hyperion, a protosupercluster at $z \sim 2.47$, provides an unprecedented opportunity to study distant galaxies in the context of their large-scale environment. We carry out deep narrowband imaging of a $\approx 1^\circ \times 1^\circ$ region around Hyperion and select 157 Lyα emitters (LAEs). The inferred LAE overdensity is $\delta_g \approx 40$ within an effective volume of $30 \times 20 \times 15$ cMpc^3, consistent with the fact that Hyperion is composed of multiple protoclusters and will evolve into a supercluster with a total mass of $M_{\rm tot} \approx 1.4 \times 10^{15}\ M_\odot$ at $z = 0$. The distribution of LAEs closely mirrors that of known spectroscopic members, tracing the protocluster cores and extended filamentary arms connected to them, suggesting that they trace the same large-scale structure. By cross-correlating the LAE positions with H I tomography data, we find weak evidence that LAEs may be less abundant in the highest H I regions, perhaps because Lyα is suppressed in such regions. The Hyperion region hosts a large population of active galactic nuclei (AGNs) ≈ 12 times more abundant than that in the field. The prevalence of AGNs in protocluster regions hints at the possibility that they may be triggered by physical processes that occur more frequently in dense environments, such as galaxy mergers. Our study demonstrates LAEs as reliable markers of the largest cosmic structures. When combined with ongoing and upcoming imaging and spectroscopic surveys, wide-field narrowband imaging has the potential to advance our knowledge in the formation and evolution of cosmic structures and of their galaxy inhabitants.

Unified Astronomy Thesaurus concepts: Galaxy evolution (594); Galaxy formation (595); High-redshift galaxy clusters (2007)

1. Introduction

Galaxy clusters provide useful cosmic laboratories to study how the large-scale environment influences the formation and evolution of galaxies. Existing observations show that cluster galaxies underwent early accelerated formation followed by swift quenching. Since then, they have been evolving passively (Stanford et al. 1998; Eisenhardt et al. 2008; Snyder et al. 2012; Martin-Navarro et al. 2018). In order to elucidate the physical processes regulating galaxy evolution and quenching, we need to rewind the cosmic clock and observe the galaxy growth in young protoclusters (i.e., structures that will eventually collapse into galaxy clusters; Overzier 2016).

Over the years, multiple techniques have been developed to identify protoclusters. These techniques include searching for overdensities of galaxies, for example, Lyman break galaxies (LBGs; Steidel et al. 1998; Intema et al. 2006; Overzier et al. 2006; Toshikawa et al. 2016, 2018), Lyα emitters (LAEs; Matsuda et al. 2005; Lee et al. 2014b; Chiang et al. 2015; Dey et al. 2016; Shi et al. 2019a), and Hα emitters (HAEs; Kurk et al. 2004; Hatch et al. 2011; Cooke et al. 2014; Shimakawa et al. 2014; Zheng et al. 2021); and rare galaxies as signposts of protoclusters such as radio galaxies (Venemans et al. 2002, 2007; Hayashi et al. 2012; Cooke et al. 2014), quasars (Wold et al. 2003; Kashikawa et al. 2007; Stevens et al. 2010; Trainor & Steidel 2012; Hennawi et al. 2015), and extended Lyα nebulae (LABs; Prescott et al. 2008; Yang et al. 2009, 2010; Badescu et al. 2017). Recently, Planck collaboration identified a large number of protocluster candidates selected as Planck point sources with colors consistent with star-forming galaxies with cold dust (Planck Collaboration et al. 2014). These approaches have achieved some success, although, in most cases, the sizes of confirmed structures are too small to enable systematic comparison (Overzier 2016; Harikane et al.

[14] Visiting astronomer, Kitt Peak National Observatory, National Optical Astronomy Observatory, which is operated by the Association of Universities for Research in Astronomy (AURA) under a cooperative agreement with the National Science Foundation.

2019). As a result, the relative overlap between samples yielded from various approaches and their selection biases remain poorly understood.

Confirming a protocluster as a galaxy overdensity is challenging due to its large cosmological distances and the expected large spatial extent of protoclusters (e.g., Chiang et al. 2013; Muldrew et al. 2015). Indeed, a handful of well-characterized systems subtend up to 10 arcmin across the sky. For this reason, it has been difficult to discern the whole extent of a protocluster and to appropriately define the galaxy's local environment. As a result, while the number of spectroscopically confirmed protoclusters has been steadily on the rise (see, e.g., Overzier 2016; Toshikawa et al. 2016, 2018; McConachie et al. 2022), the number of systems with reasonable spatial characterization remains low and mostly limited to those in a handful of deep extragalactic fields (Hayashino et al. 2004; Dey et al. 2016).

This work is motivated by the discovery and spectroscopic confirmation of Hyperion, a protosupercluster at $z \sim 2.47$ (Cucciati et al. 2018) in the COSMOS field. Extensive spectroscopy (e.g., VIMOS Ultra-Deep Survey, or VUDS; Le Fevre et al. 2015; zCOSMOS Survey: Lilly et al. 2007, 2009) and multiwavelength photometry (Laigle et al. 2016; Weaver et al. 2022) have revealed the inner structure of individual galaxy overdensities and the connectivity between them in sufficient detail. The structure is composed of multiple protoclusters and galaxy groups, which were identified by Casey et al. (2015), Chiang et al. (2015), Diener et al. (2015), and Wang et al. (2016) (hereafter, Ca15, Ch15, D16, W16, respectively). The discovery of such an immense cosmic structure and the detailed characterization of its constituents provide an unprecedented opportunity to study the formation of galaxies and protoclusters in the context of the large-scale environment.

A related question is how galaxies can be used to identify massive cosmic structures and characterize their environment. One good candidate for tracers of the large-scale structure has been LAEs (Ouchi et al. 2020). Existing studies show that LAEs tend to have low stellar masses ($\sim 10^{8\text{-}9}\ M_{\odot}$), young ages ($\sim$10 Myr), and high ratios of star formation rate (SFR) to stellar mass ($\sim 10^{-8}\ \mathrm{yr}^{-1}$, Gawiser et al. 2006; Gronwall et al. 2007; Guaita et al. 2011; Nakajima et al. 2012); they are also less dusty than any known galaxy population and hosted by moderate-mass halos (Gawiser et al. 2007; Guaita et al. 2010; Lee et al. 2014b; Kusakabe et al. 2018). These traits make LAEs the best visible tracers of the underlying matter distribution at high redshift. If LAEs are good tracers of the large-scale structure, it would follow that large-area LAE surveys may provide an effective pathway to explore the distant universe and learn about the evolution of cluster galaxies at the peak of their formation epoch.

In this work, we select a sample of LAEs fine-tuned to match the redshift span of Hyperion and study their distribution in and around Hyperion relative to the environment characterized by other tracers including spectroscopic sources (Cucciati et al. 2018), photometric redshift selected galaxies (Laigle et al. 2016; Weaver et al. 2022), H I column density (Lee et al. 2014a), and active galactic nuclei (AGNs).

This paper is organized as follows: in Section 2, we describe the observation strategy and data reduction. LAE sample selection and validation are described in Section 3. We construct the LAE spatial distribution and compare it with various tracers of Hyperion in Section 4. In Section 5, we estimate the descendant mass of the LAE overdensity and discuss the future directions in the field of cluster formation study. Finally, we summarize the main findings in Section 6. Throughout this paper, we adopt a cosmology with $\Omega_M = 0.286$, $\Omega_\Lambda = 0.714$, $h = 0.696$, $H_0 = 100\,h$ km s^{-1} Mpc^{-1}. All magnitudes are in the AB system (Oke & Gunn 1983).

2. Data and Photometry

2.1. Observations and Data Reduction

We obtained deep wide-field narrowband images using the One Degree Imager (ODI; Harbeck et al. 2014, 2018) on the WYIN 3.5 m telescope.[15] ODI has 30 orthogonal transfer array detectors arranged in a 5×6 configuration, with an intrinsic pixel scale of $0\farcs11$ pixel^{-1} and a field of view of $40' \times 48'$. Our custom narrowband filter (hereafter, NB422) has a central wavelength of $\lambda_c \approx 4225$ Å and an FWHM of 170 Å. The filter is designed to sample redshifted Lyα emission at $z = 2.40$–2.54, corresponding to a comoving line-of-sight distance of $\approx$ 170 cMpc.

The observations were carried out during four separate runs in 2018–2020 using two pointing centers: $\alpha = 10^{\mathrm{h}}01^{\mathrm{m}}25\fs5$, $\delta = +02°15'00''$ (hereafter cosmosE) and $\alpha = 09^{\mathrm{h}}59^{\mathrm{m}}25\fs5$, $\delta = +02°17'24''$ (cosmosW), J2000. These pointings overlap $0\fdg14$ in the east–west direction and together cover a total area of $\sim$0.1 deg^2 centered at $\alpha = 10h00^{\mathrm{m}}21\fs6$, $\delta = +02°14'24''$ (cosmosC). We adopted the 5ODI 9-Point dithering pattern between successive exposures to fill the gaps between CCDs. We discarded the frames with seeing $> 1\farcs3$ and the frames that were taken when the guide star was lost during the exposures. Total exposure times are 19 and 16 hr for the cosmosE and cosmosW pointings, respectively, with the overlapping region receiving the effective exposure of 35 hr. Individual exposures were 10 or 20 minutes long depending on transparency and cloud coverage.

For broadband imaging data, we utilize the existing data from the Hyper Suprime-Cam Subaru Strategic Program (HSC-SSP: Komiyama et al. 2018; Miyazaki et al. 2018) second data release (Aihara et al. 2019) and the deep u-band data from the CFHT Large Area U-band Deep Survey (CLAUDS; Sawicki et al. 2019). Both surveys cover the entire survey field imaged with NB422. Figure 1 shows the total throughput of all filters, and the filter information is summarized in Table 1. The 5σ limiting magnitudes reported by Aihara et al. (2019) are for point sources, which are $\sim$0.3 mag deeper than those measured in a $2''$ diameter aperture.

The raw images of our NB422 data are transferred and processed by the ODI pipeline, Portal and Archive (ODI-PPA; Gopu et al. 2014), where image bias, dark, and pupil ghosts are removed and the images are flat-fielded.

The astrometry is tied to the Gaia second data release (Gaia Collaboration et al. 2016) using an IRAF task `msccmatch`. After correction, the astrometric rms offsets are $0\farcs1$ for both R.A. and decl. A narrowband image with the best seeing and transparency condition is chosen as the reference image. We then resample each image with a pixel scale of $0\farcs3$ using the tangent point of the reference image using `SWarp` (Bertin et al. 2002). The scaling

[15] The WIYN Observatory is a joint facility of the NSF's National Optical-Infrared Astronomy Research Laboratory, Indiana University, the University of Wisconsin–Madison, Pennsylvania State University, the University of California–Irvine, and Purdue University.

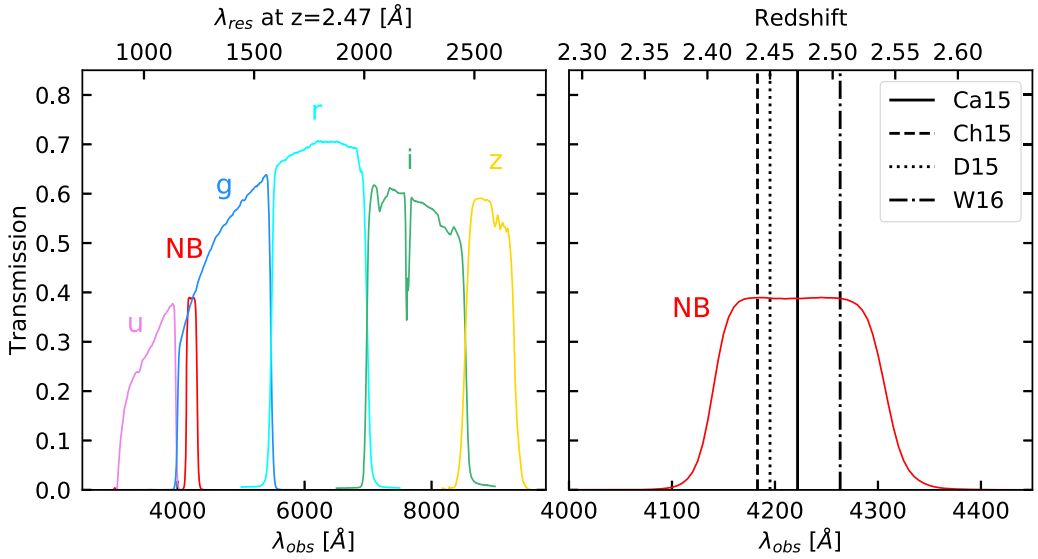

Figure 1. Left: total throughput data (including filter transmission, mirror, optics, CCD quantum efficiency) of the filters listed in Table 1. Right: closeup view of NB422 where Lyα redshift is indicated on the top axis. Vertical lines mark the redshifts of the individual protoclusters in the survey field.

Table 1
Filters Used in This Survey and Their Characteristics

Band	Instrument	$m_{5\sigma}$ [a]	FWHM
NB422[b]	WIYN/ODI	25.4	1.″0
u	CFHT/MegaCam	27.1	0.″8
g	Subaru/HSC	26.9	0.″7
r	Subaru/HSC	26.6	0.″9
i	Subaru/HSC	25.3	0.″7

Notes.
[a] 5σ limiting magnitude measured in a 2″ diameter circular aperture.
[b] We quote the measurement for the cosmosW pointing, which is shallower than cosmosE.

factor relative to the reference frame is determined by the IRAF task `mscimatch`.

Given the narrow width and the central wavelength of NB422, sky background counts in individual frames are low, requiring us to use a relatively long integration time of 20 minutes for most frames. The long exposures caused the ODI amplifiers to glow, raising the background counts in the corners of orthogonal transfer arrays closest to them. Additionally, detector cross talks produce features that are faint but extended up to a few arcseconds. We find that it is not always possible to remove these image artifacts in a systematic manner. To ensure that the final image coadd is as clean as possible, the rescaled, reprojected images are combined using a median combination method. While median stacking is not an optimal method in maximizing the image depth, it was a necessary choice given the nature of these constraints.

The final mosaic has the seeing of 1.″0. Although the image is clean and free of obvious defects, we choose not to search for extended LABs out of abundant caution that the aforementioned detector features masquerade as extended narrowband (NB) sources with no broadband (BB) counterparts. Our ability to detect point sources is affected by these detector issues.

To calibrate the photometric zero point of the final mosaic, we use the CLAUDS *u* and HSC-SSP *g* band images. To estimate continuum emission, we calculate the fractional contribution from the flux densities of *u* and *g* (denoted as *ug*) bands at the central wavelength of NB422. The zero point of the NB422 is determined by requiring that the median color excess $NB - ug$ is zero for all objects with $0 \leqslant g - r \leqslant 1.0$.

2.2. Photometry

In order to construct a multiwavelength photometric catalog, we first calibrate the astrometry of each broadband image with the Gaia DR2 data. We also match the pixel scale of all images to that of the NB422 image 0.″3 pix^{-1}; the broadband data from the SSP and CLAUDS surveys have the pixel scale of 0.″168 pix^{-1}. We homogenize the point-spread functions (PSFs) of the broadband data with the seeing of the NB422 image. A Moffat profile is assumed to fit the PSF of each image with a measured seeing and a fixed parameter $\beta = 3$. The convolution kernel is obtained from an IDL routine `MAX_ENTROPY`. Each broadband image is then convolved with the respective kernel to create the PSF-matched image.

We run `SExtractor` (Bertin & Arnouts 1996) on a dual-image mode to create a multiwavelength catalog where the NB422 image is used for detection (`DETECT_THRESH` = 1.1, `MIN_AREA` = 10). Photometry is performed in all images. Colors are estimated from isophotal flux (`FLUX_ISO`). A total of 64,690 sources are detected.

3. Analysis

3.1. Lyα Emitter Selection

In the right panel of Figure 1, we show the NB422 filter transmission. The redshifts of the four largest protoclusters within Hyperion are indicated as vertical lines, illustrating that any Lyα-emitting galaxies that belong to these structures should lie well within the filter transmission. LAEs are selected using the following criteria:

$$\Sigma_s \geqslant 2 \bigcap \mathrm{S/N(NB422)} \geqslant 10 \bigcap \mathrm{NB422} - g \leqslant -0.5, \quad (1)$$

where Σ_s is the flux density excess measured relative to the 1σ photometric scatter expected for zero NB422 $- g$ color and S/N is the signal-to-noise ratio within the isophotal area. The

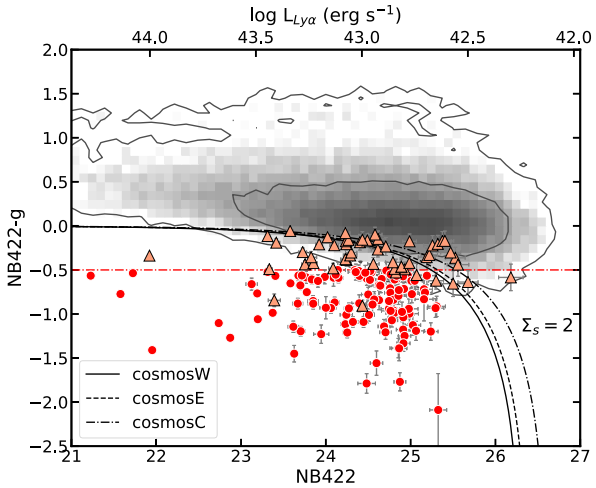

Figure 2. NB422 − g color as a function of NB422 magnitude. All NB422 sources are represented by the gray scale and the contour lines. Photometric LAE candidates (pLAEs) selected using Equations (1) and (3) are shown as circles; triangles indicate the $z_{\rm fig3} = 2.40$–2.52 sources satisfying the same criteria with a modified line excess $\Sigma_s > 1$ (sLAEs). The solid, dashed, and dashed–dotted curves show the $\Sigma_s = 2$ lines computed for the cosmosW, cosmosE, and cosmosC subfields, respectively. The horizontal dashed line marks the color corresponding to a rest-frame equivalent width $W_0 = 50$ Å at $z = 2.45$.

color cut NB422 − $g = -0.5$ corresponds to the rest-frame equivalent width $W_0 = 50$ Å. Since our NB422 and g-band data are dominated by background noise, we expect both photometric error and Σ_s to vary as a function of color:

$$m_g - m_{\rm NB} = -2.5\log_{10}(1 - \Sigma_s 10^{-0.4(ZP - m_{\rm NB})}\sqrt{\sigma_g^2 + \sigma_{\rm NB}^2}), \quad (2)$$

where ZP is the photometric zero point of the NB422 image. Finally, at $z \sim 2.5$, the Lyman limit is redshifted to $\lambda_{\rm obs} \sim 3200$ Å, resulting in the flux deficit in the u band. Instead of using the color purely based on the intergalactic H I absorption, we fine-tune the $u - g$ color criterion based on those of the spectroscopic sources at $z_{\rm spec} = 2.4$–2.7 and require

$$u - g \geqslant 0.9 \times (g - r) - 0.2. \quad (3)$$

In Figure 2, we show the NB422 − g color versus the narrowband magnitude of all NB-detected sources. The line-excess criterion applied to each field is shown as black curves.[16] In principle, our selection criteria (Equations (1)–(3)) could lead to a higher LAE source density in the overlapping region (cosmosC) than that outside it. However, it is clear in Figure 2 that the stringent color cut ($NB422 - g \leqslant -0.5$) and the S/N requirement primarily drive the LAE selection and that the fluctuation of Σ_s across the field has little impact on the sample selection. We select 114 LAEs based on our photometric selection criteria and refer to them as pLAEs throughout this paper.

Utilizing extensive spectroscopy available in the field, we select 53 sources at $z_{\rm spec} = 2.40$–2.54 requiring a less stringent line excess of $\Sigma_s \geqslant 1$: that is, NB422 − g colors are still consistent with having Lyα emission but at a lower equivalent width. We refer to these galaxies as sLAEs. As expected, the majority of the sLAEs have redder NB422 − g colors than the pLAEs (orange triangles in Figure 2). A few are too faint and missed by our pLAE selection because they fail to meet any of the S/N, NB422 − g, or $\Sigma_s \geqslant 2$ requirements. There are a handful of sLAEs that satisfy our selection criteria but are excluded because they are close to bright stars or image boundaries. Of the 53 sLAEs, 51 come from the VUDS and zCOSMOS surveys, which cover the region uniformly. The remaining two come from the HETDEX Pilot Survey (HPS; Adams et al. 2011; Chiang et al. 2015), whose coverage is indicated in the right panel of Figure 4 by a yellow polygon.

To summarize, we have selected 114 pLAEs and 53 sLAEs by combining the photometric and spectroscopic catalogs. The pLAEs represent higher-EW LAEs selected purely based on photometric criteria, while sLAEs are spectroscopic sources at the Hyperion redshift range with weaker but distinct Lyα emission. All together, our sample consists of 167 LAEs.

3.2. Multiwavelength and Spectroscopic Data

To validate our sample selection and to quantify the rate of contamination, we compile the existing multiwavelength and spectroscopic data in the field. For spectroscopy, we merge the redshift catalogs from the zCOSMOS survey (Lilly et al. 2007, 2009) and the VIMOS UltraDeep Survey (VUDS; Le Fevre et al. 2015). We will refer to the merged catalog as the VUDS+zCOSMOS catalog hereafter. The same catalog was used in Cucciati et al. (2018).

Sample Contamination. At the central wavelength of our NB422 filter, the dominant contaminants of the LAE selection are expected to be [O II] emitters at $z = 0.13$, but the contamination is likely low. At $z = 0.13$, the volume covered by our data is negligibly small at ≈0.8% compared with that at $z \sim 2.5$. Ciardullo et al. (2013) found that at $z < 0.2$, [O II] emitters have a rest-frame equivalent width of $W_{0,[\rm O\ II]} = 8 \pm 2$ Å. Our NB422 − g color cut corresponds to an observed equivalent width of 170 Å and thus excludes most [O II] emitters. Assuming that [O II]λ3727 emitters have an equivalent width distribution similar to that measured by Ciardullo et al. (2013), we expect $\lesssim$1 galaxy at $z < 0.2$. Indeed, none of our pLAEs are classified as [O II] emitters in the spectroscopic catalog.

Low-luminosity AGNs with a broad-line emission can also contaminate our LAE sample. We cross-match the LAEs with the source lists from the Chandra COSMOS Legacy Survey (Civano et al. 2016; Marchesi et al. 2016) and the XMM-LSS survey (Chiappetti et al. 2005) and find that 24 LAEs have X-ray detections. Of these 24, seven with spectroscopic redshifts at $z_{\rm spec} < 2.40$ are removed from our LAE sample. Their blue NB422 − g colors are likely a result of broad C IV, Fe II, and O II emission lines falling into the NB422 filter (Vanden Berk et al. 2001). Of the remaining 17, 16 lie within the NB422 redshift range and one LAE has no spectroscopic match. The spatial distribution of these 17 X-ray LAEs is discussed in Section 4.5.

We also cross-match the source list with the Spitzer MIPS 24 μm catalog (Sanders et al. 2007) and the radio data from the 1.4 GHz Very Large Array (VLA)-COSMOS survey (Schinnerer et al. 2010) and find four and eight matches, respectively. At $z \approx 2.5$, 24 μm samples $\lambda_{\rm rest} \approx 7$ μm emission of dust heated by starbursts or AGNs (Coppin et al. 2010). The radio emission is produced by synchrotron radiation from relativistic jets of

[16] The sky background noise $\sigma_{\rm NB}$ is estimated separately for the cosmosW ($\alpha < 150.^{\circ}02$), cosmosE ($\alpha \geqslant 150.^{\circ}02$), and the overlapping region, cosmosC. We obtain $\sigma_{\rm NB} = 1.08$, 1.01, and 0.81 erg s^{-1} cm^{-2} Hz^{-1} in cosmosW, cosmosE, and cosmosC, respectively.

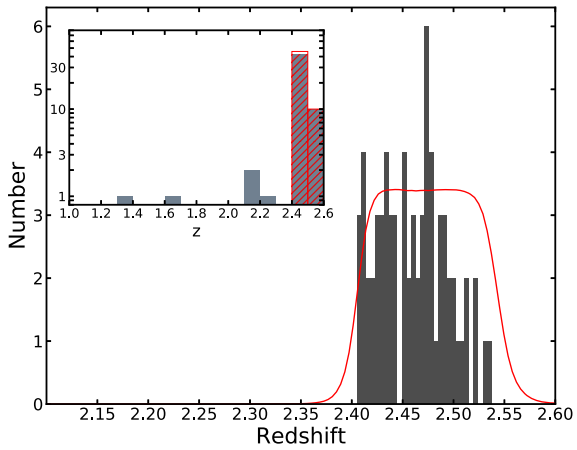

Figure 3. The spectroscopic redshift distribution of the 70 LAEs with spectroscopic counterparts in the redshift range is shown. The red curve shows the NB422 filter transmission with arbitrary normalization. The inset shows the zoomed-out distribution including 5 low-z redshift interlopers. The red hatched bars highlight those at Hyperion redshift.

supermassive black holes (Blandford & Payne 1982; Bridle & Perley 1984). Two MIPS sources and three radio counterparts are spectroscopically confirmed to be within our redshift range. The remaining ones have no spectroscopic detection.

Several LAEs are flagged as AGNs by multiple diagnostics. LAE_31446 ($z_{\rm spec} = 2.450$) is detected at X-ray, mid-IR, and radio wavelengths. LAE_8845 (MIPS and radio), LAE_20628 (X-ray and MIPS), and LAE_3575 and LAE_34108 (X-ray and radio) also have multiple detections. All lie within the NB422 redshift range except for LAE_33546 ($z_{\rm spec} = 2.146$).

Regardless of the AGN content, we retain all sources that lie within the NB422 redshift range and also retain six sources with no spectroscopic redshift. After removing seven sources at $z_{\rm spec} < 2.40$, our catalog contains 160 LAEs (107 pLAEs and 53 sLAEs).

Redshift Distribution. Using the VUDS, zCOSMOS, and HPS spectroscopic catalogs, we validate our LAE selection. We only use sources with reliability $\gtrsim$75% according to their redshift flag;[17] for the HPS sources, we use all sources in the COSMOS field because no redshift quality flag is available (Adams et al. 2011). In Figure 3, we show the redshift histogram of the LAEs with spectroscopic counterparts. The main panel shows the redshift distribution of our LAEs after removing low-z interlopers, while the inset shows a broader distribution including them. Nearly half (75) of our LAEs have spectroscopic redshifts. Of these, 70 lie at $z_{\rm spec} = 2.40$–2.54, consistent with that expected from the filter transmission curve (red curve). Among the five lower-z interlopers, three are broad-line AGNs identified by VUDS, which we remove from our LAE catalog.

We estimate the purity of our photometric pLAE sample, defined as the fraction of selected sources that fall within the expected redshift range regardless of their spectral types. Of the 27 pLAEs, 22 are confirmed at $z_{\rm spec} = 2.40$–2.54 and 5 at $z_{\rm spec} < 2.4$. Thus, the purity of the pLAE sample is 77%, comparable to the value found by other LAE surveys at $z = 2$–6 (e.g., Ouchi et al. 2008; Nakajima et al. 2012). Our final catalog contains 157 LAEs, which include 104 pLAEs and 53 sLAEs.

[17] The redshift reliability flag equal to X2, X3, X4, or X9. $X = 0$ is for galaxies; $X = 1$ is for broad-line AGNs; $X = 2$ and $X = 3$ are the cases where secondary objects fall in the slit and are separable/not separable from the main target (Le Fevre et al. 2015).

4. Large-scale Structure Traced by LAEs

4.1. The Sky Distribution of LAEs

Our sample consists of 157 LAEs over the survey area of 3,455 arcmin^2, yielding the mean surface density of $\bar{\Sigma} = (4.5 \pm 0.4) \times 10^{-2}$ arcmin^{-2} where the uncertainty reflects the Poisson noise. Using this number as the baseline, we quantify the distribution of local over- and underdensities traced by the LAEs. The 2D distribution is constructed using a PYTHON function `hist2D` and then smoothed with a Gaussian kernel of an FWHM 10 cMpc. The kernel size is chosen to maximize the density contrast of a protocluster and is comparable to those adopted in the literature for LAE overdensity identification (Badescu et al. 2017; Shi et al. 2019a). The LAE density map is shown in the left panel of Figure 4 where both contours and gray scale represent the local surface density relative to the field average. The positions of the pLAEs and sLAEs are shown as circles and triangles.

A significant LAE overdensity lies at the center of the field. Taking the $2.0\bar{\Sigma}$ isodensity contour as the boundary, the area of the overdensity is 226.4 arcmin^2 in which 38 LAEs are enclosed. The number density of LAEs in the region is 0.17 ± 0.03 arcmin^{-2}, a factor of 3.7 ± 0.5 times the field average (the overdensity, calculated as $\delta_\Sigma \equiv (\Sigma/\bar{\Sigma} - 1)$, is 2.7 ± 0.5). The likelihood of such an overdensity arising from Poisson fluctuation is $\sim 10^{-11}$. Since the galaxy surface density, $\bar{\Sigma}$, is strongly affected by the existence of the overdensity, we recompute both field LAE density and the central overdensity after excluding the overdensity region, which are $\bar{\Sigma} = (3.7 \pm 0.3) \times 10^{-2}$ arcmin^{-2} and $\delta_\Sigma = 3.6 \pm 0.7$, respectively.

Over our survey field, a large fraction of our LAEs have known redshifts from various spectroscopic surveys. Indeed, the number of sLAEs is not negligible compared to that of pLAEs within the central overdensity. To demonstrate that the presence of the overdensity is robust regardless of the inclusion of the spectroscopic sources, we repeat the same procedure but this time only using pLAEs, that is, the sources that satisfy our LAE criteria (Equations (1) and (3)). Our result, shown in the right panel of Figure 4, suggests that the same general region stands out as a pLAE overdensity. Similar to previously, the $2.0\bar{\Sigma}$ isodensity contour has the effective area of 228.4 arcmin^2 within which 27 pLAEs are found. The central overdensity is $\delta_\Sigma = 3.8 \pm 0.8$, similar to our estimate that was made including both pLAEs and sLAEs. Both pLAEs and sLAEs broadly trace the same cosmic structure.

4.2. LAE Overdensity versus Hyperion

In this section, we consider the LAE distribution in the context of the large-scale environment in and around Hyperion traced by (primarily) more massive star-forming galaxies. Even though we do not know the true underlying matter distribution, spectroscopic identification of galaxies in principle should allow a more inclusive selection in a densely sampled spectroscopic field such as COSMOS. We begin by comparing our LAEs with the density field of Hyperion measured by Cucciati et al. (2018) and then subsequently with those of the individual protoclusters identified therein (Casey et al. 2015;

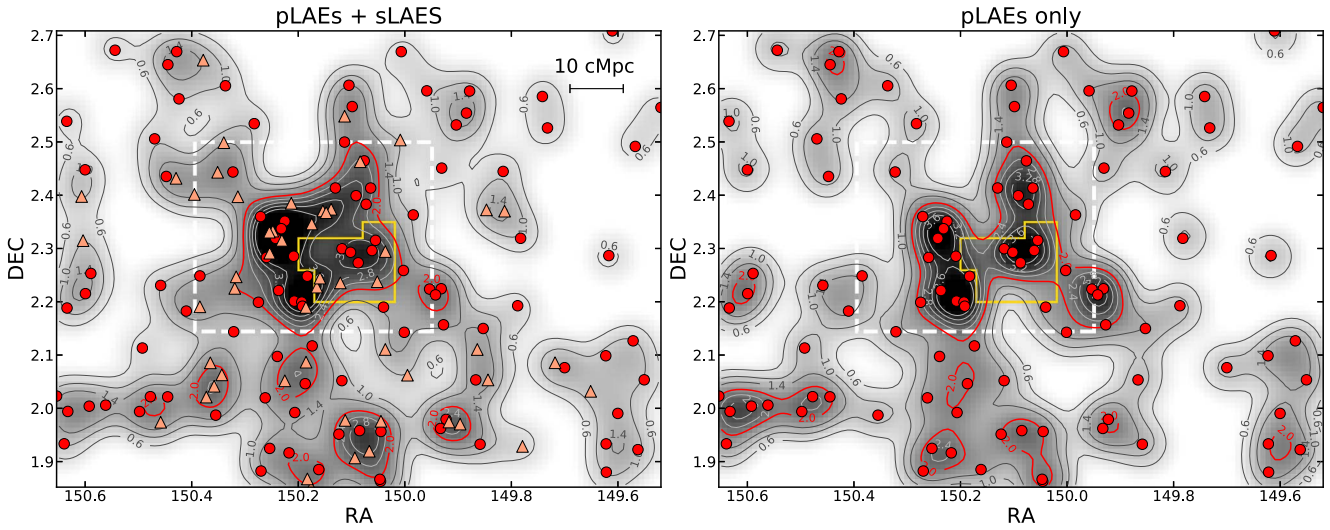

Figure 4. Left: smoothed density map of LAE candidates at $z = 2.47$. Red circles and salmon triangles represent pLAEs and sLAEs, respectively. The contours and background gray scale show the surface density levels relative to the field, and the red highlighted contour ($2.0\bar{\Sigma}$) marks the threshold for protocluster selection. The yellow thick polygon shows the field of view of the HPS survey. The white dashed rectangle shows the field of view of the CLAMATO survey. Right: smoothed density map constructed by pLAEs only.

Chiang et al. 2015; Diener et al. 2015; Wang et al. 2016). In both cases, spectroscopy largely comes from the VUDS and zCOSMOS surveys. The VUDS survey area is indicated by a gray dashed polygon in the top right panel of Figure 5, while the zCOSMOS coverage is uniform within our survey field.

The density field of Hyperion is estimated by combining the spectroscopic members and photoz member candidates and performing the two-dimensional Voronoi tessellation on their positions, resulting in a measure of the local surface overdensity, $\delta_{\rm gal,C18}$. We refer interested readers to Cucciati et al. (2018) for details. The extent of Hyperion is then defined as a contiguous region that rises above $2\sigma_\delta$, where σ_δ is the standard deviation of $\log(1+\delta_{\rm gal,C18})$, which is assumed to be a normal distribution. Additionally, they identified seven individual structures whose density peaks rise above $5\sigma_\delta$ from the mean density. In the top left panel of Figure 5, we show the projected bounds of Hyperion (black dashed line) and its seven peaks (solid color contours). Each line corresponding to a peak is color-coded by redshift indicated by the color bar.

The extent of the LAE overdensity (indicated by red contours in Figure 5) is nearly entirely enclosed by the much larger bounds of Hyperion. Both distributions also feature similar filamentary arm–like features stretching out from the main body, two northward and the third in the northeast-southwest direction. These features will be discussed later. Four of the seven Hyperion peaks reside inside or significantly overlap with the LAE overdensity contour (cyan, green, and darker orange contours in the top left panel of Figure 5). The lowest redshift peaks (blue contours) do not have LAE counterparts possibly because their redshift ranges lie near the blue cutoff of the NB422 transmission (Figures 1 and 3).

The four structures lying inside the LAE overdensity largely overlap with individual protoclusters reported by Ch15 and D16 ($z = 2.44$–2.45), D16 ($z = 2.47$), and W16 ($z = 2.50$). In Figure 5 (the top right panel and the bottom panels), we plot the spectroscopic sources within the redshift range[18] of each protocluster to discern their angular extent individually. Galaxy members published in these discovery papers are indicated as triangles, while all other spectroscopic sources are shown as squares, both color-coded by redshift. The corresponding density peak identified by Cucciati et al. (2018) is shown as a color contour. In what follows, we utilize these figures as a visual guide and discuss the angular distribution of our LAEs in the context of Hyperion protoclusters.

4.2.1. LAEs in Ch15 and D16 structures (z = 2.440–2.450)

Figure 5 (top right) shows that the main structure whose center position is $(\alpha,\ \delta,\ z) = (149.^\circ50,\ 2.^\circ25,\ 2.444)$. It is elongated stretching in the northeast–southwest direction with a smaller group of galaxies at ≈10 cMpc east of it. This configuration is closely mirrored by the LAEs, which extend further in the southwestern direction and form a compact group on the eastern end of the overdensity. The structure coincides with two protoclusters identified by Ch15 and D16. The two protoclusters are close in both redshift and angular space and thus are likely a single broad structure.

The protocluster at $z = 2.44$ was first reported by Ch15 as a concentration of nine LAEs from the HPS survey, while the $z = 2.45$ structure was initially identified by the zCOSMOS survey as one of the 42 galaxy protogroups at $z = 1.8-3.0$; based on the VLT/FORS2 spectroscopy, D16 reported 11 spectroscopic member galaxies.

Six of the nine Ch15 sources are recovered by our LAE selection. Of the remaining three, two have $\mathrm{NB422} - g > 0.2$ colors and the third has no NB422 detection. Given the large size of the fibers ($4.''2$), these sources may have been mismatched to other galaxies. Alternatively, they may be serendipitous detection of fainter galaxies. None of the D16 sources are LAEs; they are bright at near-infrared wavelength ($K_s < 24.0$), suggesting that they represent more evolved, more massive galaxies than our LAEs.

4.2.2. LAEs in the D16 structure (z = 2.465–2.475)

Two *Hyperion* density peaks lie at $z \approx 2.47$ with the center positions $(\alpha,\ \delta,\ z) = (150.^\circ09,\ 2.^\circ40,\ 2.468)$ and $(150.^\circ26,\ 2.^\circ34,$

[18] Since Cucciati et al. (2018) used 2D Voronoi tessellation in successive redshift bins, the redshift range we adopt here is unlikely to be identical to that used in their analyses.

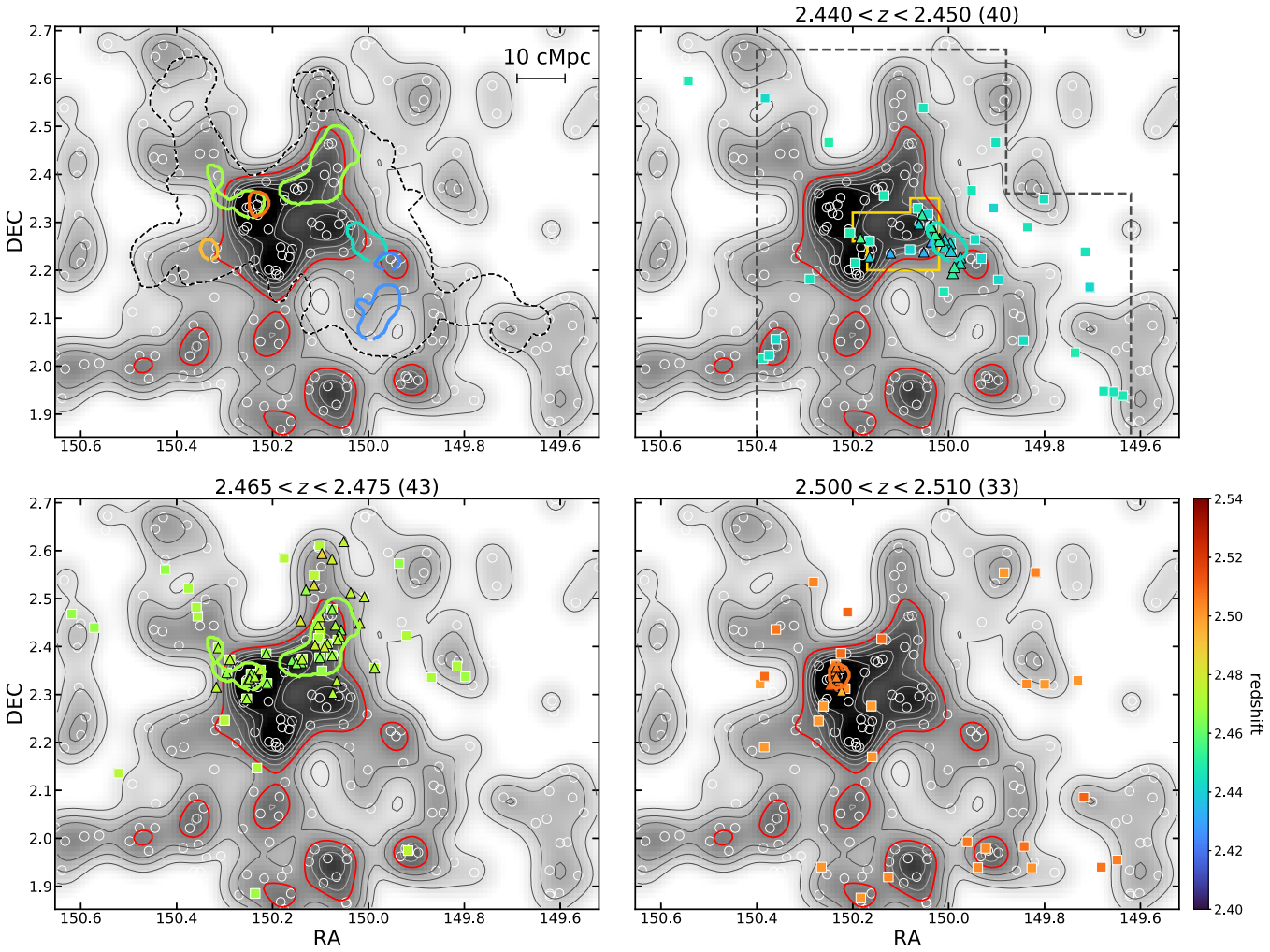

Figure 5. The sky distribution of all LAEs (white open circles) in the context of Hyperion. The extent of Hyperion reported by Cucciati et al. (2018) is shown in the top left panel as a black dashed line with the known spectroscopic members marked as triangles. The color contours represent the seven density peaks of Hyperion color-coded by their redshifts, of which the four largest protocluster members are those reported by Ch15 and D16 (top right), D16 (bottom left), and W16 (bottom right). The redshift range of these individual protoclusters and their number of spectroscopic sources are found at the top of each panel; these galaxies are plotted as squares. The smoothed LAE density maps in the background are identical to that shown in the top left panel of Figure 4. The region covered by VUDS and HPS is marked in the top right panel as dark gray and gold dashed polygons, respectively. All spectroscopic sources are color-coded by redshift as indicated by the color bar.

2.469). The structure was initially discovered by D16 as an overdensity of dusty star-forming galaxies (DSFGs) at $z = 2.47$. Extensive follow-up spectroscopy revealed 41 galaxy members including 33 LBGs, seven DSFGs, and one quasar. Only nine of these members are recovered by our LAE selection, consistent with the fact that dusty or UV-luminous galaxies tend not to be strong line emitters.

Similar to the D16 structure, the member galaxies form a linear structure stretching out in the north–south direction. However, the full spectroscopy of the region revealed another long array of galaxies in the east, nearly parallel to the main body. The two are joined together at the northern end of the LAE overdensity, forming a letter *U*. As such, it appears that the $z \approx 2.47$ structure possibly traces two large overdensities each with a filamentary arm. Once again, the LAEs trace the spectroscopic members remarkably well; the contour lines clearly mark the locations of the two filaments stretching northward, and the two main overdensities of the $z \approx 2.47$ structure lie well inside the LAE overdensity.

4.2.3. LAEs in the W16 structure (z = 2.500–2.510)

One of the most compact peaks of Hyperion is located at (α, δ, z) = (150°.23, 2°.34, 2.507). W16 initially reported this structure as a highly significant (11.6σ) overdensity of distant red galaxies. Many are populated in a compact region $\approx$10″ in diameter ($\approx$80 kpc physical). The region shows weak extended X-ray emission detected by Chandra, suggesting a possible presence of a hot protointracluster medium. Seventeen massive galaxies ($M_{\rm star} \gtrsim 10^{10.5}\ M_{\odot}$) are confirmed as spectroscopic members via Atacama Large Millimeter/submillimeter Array and near-IR spectroscopy. Although individually plotted, their locations appear as a single symbol in Figure 5 (bottom right) due to their proximity.

Although the LAE overdensity peaks near the highest concentration of DSFG members, it remains unclear how many of the LAEs belong to $z \approx 2.50$. As can be seen in the top left panel of Figure 5, the region is home to two galaxy overdensities (at $z \approx 2.47$ and $\approx$2.50). By cross-matching the positions of LAEs with the VUDS/zCOSMOS catalog, we find

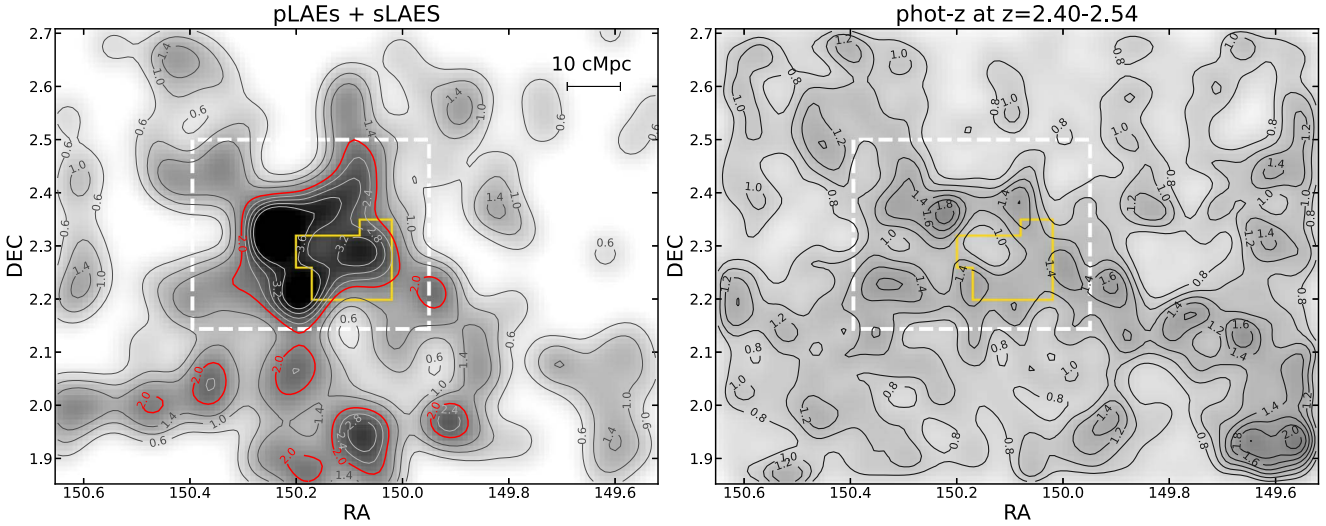

Figure 6. Left: smoothed density map of LAE candidates at $z = 2.47$. The contours and background gray scale are identical to the left panel of Figure 4. The yellow thick polygon shows the field of view of the HPS survey. The white dashed rectangle shows the field of view of the CLAMATO survey. Right: smoothed density map using selected photometric galaxies in the COSMOS2015 catalog (Laigle et al. 2016).

that two LAEs are found in the outskirts of the structure at $z = 2.53$, while the remainder is at $z = 2.47$. Our visual inspection also suggests the least correlation between the spectroscopic sources and the LAEs.

The dearth of LAEs associated with the W16 structure is in stark contrast with all other protoclusters in the region. Given the tentative X-ray detection and the excess of evolved galaxy populations in the region, it is possible that, in the most massive halo, the formation of low-mass line emitters is already suppressed (see Section 4.4). However, the relative lack of LAEs in the extended region around the core is more difficult to explain.

In addition to the association of LAEs with individual protoclusters, we also perform the Spearman's rank correlation test to determine how well LAEs trace the spec-z sources. To this end, we use the `scipy.stats.spearmanr` routine in PYTHON, limiting the sources to lie within the region $\alpha_{2000} = 150.^{\circ}00$–$150.^{\circ}45$ and $\delta_{2000} = 2.^{\circ}15$–$2.^{\circ}50$. The redshift range is chosen to be 2.40–2.54 to reflect the redshift selection function defined by the NB422 transmission (Figure 3); only the spectroscopic sources with redshift reliable flag larger than 2 are used. The resultant galaxy samples are then binned to construct a 2D histogram with each cell 16″ on a side. We obtain the Spearman's coefficients $\rho = 0.27$ and $p = 8.09 \times 10^{-31}$ for the full LAE sample: that is, the likelihood that the two distributions are correlated ($\rho > 0$) is extremely high at $1 - p$. Since the sLAEs are selected in part because they lie at this redshift range, we also repeat the test by only using pLAEs and obtain $\rho = 0.06$ and $p = 0.012$. While the significance is lower, the result suggests that the two distributions are correlated at a 2.5σ level. The similarities in the LAEs versus spectroscopic sources strongly hint that the LAEs are excellent tracers of the large-scale structure within massive protoclusters.

4.3. Environment Measured by Photometric Redshifts

Using the public COSMOS2015 catalog (Laigle et al. 2016), we characterize the large-scale environment traced by photometric galaxies. Although photometric redshift precision is poorer than that achievable by spectroscopy and narrowband imaging, the catalog provides more than half a million galaxies, thereby substantially lowering the Poisson fluctuations of local density measurements. Additionally, the measurements of SFR and stellar masses of each galaxy can elucidate the evolutionary stages of galaxies within the structure. Indeed, several studies used the photoz technique to identify protoclusters (Toshikawa et al. 2012; Chiang et al. 2014; Toshikawa et al. 2016) or to study the density-SFR relation (Koyama et al. 2013; Cooke et al. 2014) at high redshift.

The COSMOS2015 sources are selected based on the UltraVISTA DR2 survey $YJHK_S$ bands. The catalog also includes a suite of deep optical data from CFHT and Subaru and the Spitzer IRAC 3.6/4.5 μm data from the Spitzer Large Area Survey with Hyper-Suprime-Cam (SPLASH) survey. Although several strips covering an area of 0.6 deg^2 were imaged at a greater depth ($K_S = 24.7$ AB, 3σ, 3″), we limit our analysis to the sources brighter than $K_S = 24$ to ensure uniformity across the field, roughly corresponding to $M_{\rm star} \gtrsim 10^{10} M_{\odot}$ at $z = 2.5$. When compared against the zCOSMOS and VUDS spectroscopic sources at $z > 1.5$, we find the redshift uncertainty to be $\sigma_{\Delta z}/(1 + z_s) \sim 0.03$ and the catastrophic failure ranges to be between 8% and 13%, respectively.

To construct the local density map, we treat each galaxy's redshift in a probabilistic manner, that is, the probability density function (PDF) of a given galaxy obeys a normal distribution centered on $z = $ `zPDF`; the standard deviation is computed as one-half of the distance between the upper and lower 68% confidence level (`zPDF_h68` and `zPDF_l68`). We assign a redshift to each galaxy accordingly but only retain galaxies at $z = 2.40$–2.54, typically resulting in ≈2000 galaxies in the 1.5 deg^2 UltraVISTA field. Using these galaxies, the local density map is constructed in an identical manner as in Section 4.1. This procedure is repeated 10,000 times, and the final density map is computed as the average over all realizations and is visualized in the right panel of Figure 6.

The photoz density map reasonably matches several features present in the LAE overdensity map, including the highest galaxy overdensities within Hyperion and the voids around it. However, the features reminiscent of "filaments" present in both LAE and spectroscopic distributions are largely missed by the photoz density map; this is not surprising given that these

regions are intermediate in the density range and thus are more likely to be washed away by the large photoz uncertainties. Additionally, the most significant photoz overdensity—located at the southwestern corner near (α, δ) $\approx$ (149.°6, 1.°9)—does not have a counterpart in the LAE overdensity. The same structure was identified by Chiang et al. (2014), constructed from an earlier version of the COSMOS photometric redshift catalog. The nature of this galaxy overdensity is unknown. It could be a protocluster at a slightly lower or higher redshift than Hyperion such that Lyα emission from its star-forming members falls outside our filter bandpass.

In order to quantify how well LAEs trace the photoz sources, we perform the Spearman's rank correlation test in an identical manner as in Section 4.2. We compare the distribution of all LAEs to the unsmoothed photoz density map averaged over 10,000 random realizations within the region $\alpha_{2000} =$ 150.°00–150.°45 and $\delta_{2000} = 2.°15$–$2.°50$. We obtain the Spearman's coefficients $\rho = 0.06$ and $p = 0.023$, that is, the two distributions are correlated at a 2.3σ significance level. Given the relatively large redshift uncertainty expected for the photometric redshifts of sources, it is reasonably expected that LAEs and photoz trace the same large-scale structures.

We repeat the same analysis using the COSMOS2020 catalog (Weaver et al. 2022), an updated version of the COSMOS2015 catalog with an improved photometric redshift precision ($\sigma_{\Delta z}/(1+z_s) \lesssim 0.025$ and the catastrophic failure $\lesssim$8%) and find a nearly identical result.

In conclusion, a photometric redshift technique offers a promising avenue of identifying distant protoclusters, but its estimate of local density needs to be taken with caution. Additionally, the regions of interest such as filaments connecting to high-density knots are more clearly traced by line-emitting galaxies.

4.4. The Distribution of LAEs versus H I Gas

We compare the LAE distribution with the H I gas distribution as measured by the COSMOS Lyman-Alpha Mapping and Tomography Observations survey (CLAMATO; Lee et al. 2014a). CLAMATO measured Lyα forest absorption in the spectra of background quasars and star-forming galaxies at $z = 2.3-2.8$ in the region surrounding Hyperion (see Figure 4). The Lyα forest fluctuation is defined as $\delta_F \equiv F/\langle F_z \rangle - 1$, where F is the Lyα transmission relative to the continuum and $\langle F_z \rangle$ denotes the mean transmission as a function of redshift from Faucher-Giguere et al. (2008). CLAMATO reconstructed the Lyα forest fluctuation, $\delta_F^{\rm rec}$, calculated from δ_F corrected by the noise covariance matrix with the spatial resolution of 5 cMpc at $z = 2.05$–2.55.

To determine the Lyα forest fluctuation at the angular positions of LAEs, we project the 3D CLAMATO data to our survey redshift range $z = 2.40$–2.54. We denote $\delta_{F,\rm 2D}^{\rm rec}$ as the reprojected Lyα forest fluctuation, while $\delta_{F,\rm 3D}^{\rm rec}$ refers to the 3D CLAMATO data cube. In both cases, negative $\delta_F^{\rm rec}$ values mean stronger than average Lyα absorption (i.e., high hydrogen column density).

The top left panel of Figure 7 shows the 2D gas density map where the LAE surface density contours are overlaid. In the bottom left panel, we compare the $\delta_{F,\rm 2D}^{\rm rec}$ distributions on the positions of LAEs (red) and spectroscopic members of Hyperion at $z = 2.40$–2.52 (green). We also show the rescaled $\delta_{F,\rm 2D}^{\rm rec}$ distribution of 10,000 galaxies at random positions within the field as a reference (gray).

The result shows similar mean values: $\delta_{F,\rm 2D}^{\rm rec} = -0.03$, -0.02, and -0.03 for the LAEs, spec-z galaxies, and random galaxies, respectively. This is likely because the 2D projection washes away the density fluctuations occurring at protocluster scales ($\Delta z \sim 0.01$ or $r \sim 10-15$ cMpc) as reported by Lee et al. (2016). NB422 covers a much larger line-of-sight distance of $\approx$170 cMpc.

We repeat the same analysis but this time using 29 LAEs that have the CLAMATO data coverage and spectroscopic confirmation to examine the 3D distribution. Random points are drawn in the 3D volume. The bottom right panel of Figure 7 shows that the locations of LAEs and spectroscopic galaxies are skewed toward more negative $\delta_{F,\rm 3D}^{\rm rec}$ values (-0.08 and -0.16, respectively), suggesting that both are preferentially found in H I-overdensity regions. The random distribution peaks at ≈ 0 as expected. While the $\delta_{F,\rm 3D}^{\rm rec}$ distribution peaks at similar values for both LAEs and spec-z sources, the latter is skewed toward higher H I column densities than the former. The Anderson-Darling test suggests the distributions of $\delta_{F,\rm 3D}^{\rm rec}$ may be statistically different for LAEs and spec-z sources at the $\approx 1.8\sigma$ ($p = 0.07$) significance level. Our result hints at the possibility that LAEs systematically avoid the regions of the highest gas densities (see Figure 7, top left). A larger spectroscopic sample is needed to unambiguously discern this trend.

Existing observations show a positive correlation between intergalactic medium (IGM) opacity and galaxy density on megaparsec scales (Adelberger et al. 2003; Lee et al. 2016; Newman et al. 2020). Our result appears to suggest, to the contrary, that LAEs tend to avoid the regions with the highest hydrogen column densities. Our finding is consistent with the findings of Momose et al. (2021), who measured the cross-correlation function between galaxy number density and IGM traced by Lyα forest absorption using the CLAMATO data in conjunction with 19 LAEs at $z_{\rm fig3} = 2.125-2.225$. They reported a "flattening" of the positive LAE-IGM correlation at scales $\lesssim$several cMpc, hinting that LAEs are not found in the highest gas and dark matter density. While more observations are needed to quantify this effect at a higher significance, our result is consistent with the expectation that Lyα transmission via resonant scattering declines precipitously with the gas column density.

4.5. The Prevalence of AGN near the LAE Overdensity

It is widely accepted that AGNs may play an important role in regulating star formation in galaxies (Hopkins et al. 2014; Somerville & Dave 2015; Beckmann et al. 2017; Penny et al. 2018). At low redshift, existing observations suggest that the level of AGN activity is low in a high-density environment where galaxies tend to be passively evolving (Gisler 1978; von der Linden et al. 2010; Mo et al. 2018). There is a hint that the AGN–galaxy density relation may reverse at higher redshift (Lehmer et al. 2009; Digby-North et al. 2010; Alberts et al. 2016; Krishnan et al. 2017) following the reversal of the SFR–density relation (e.g., Cooper et al. 2008; Shimakawa et al. 2018; Lemaux et al. 2022). In this section, we examine the distribution of AGNs in relation to the LAE density in and around Hyperion.

As discussed in Section 3.2, a number of LAEs are classified as AGN based on X-ray, radio, and mid-IR observations. Additionally, existing spectroscopy identified a number of broad-line AGNs at $z = 2.40$–2.54. While sources outside the

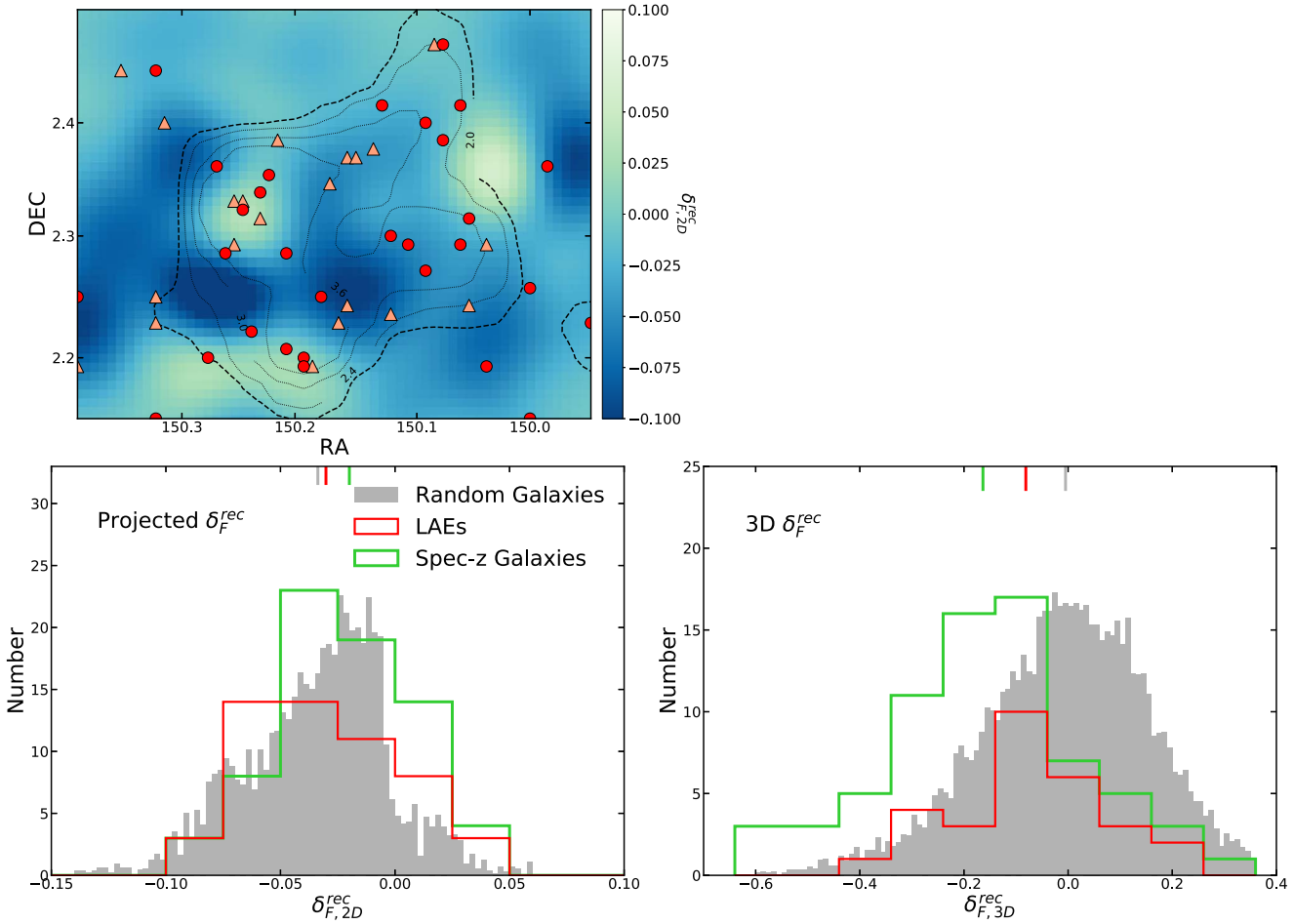

Figure 7. Top left: the sky distribution of the LAEs within the CLAMATO field of view. Red circles and salmon triangles mark the position of pLAEs and sLAEs, respectively. The contours label the galaxy number density, and the dashed contour highlights the central overdensity. The background color map shows the projected Lyα forest fluctuations $\delta_{F,2D}^{rec}$ over redshift $z = 2.40-2.54$. Bottom left: histograms of $\delta_{F,2D}^{rec}$ of all LAEs (red steps), spectroscopic members of the Hyperion (green steps), and random galaxies (gray bars). The mean $\delta_{F,2D}^{rec}$ value of each sample is shown at the top axis. Bottom right: histograms of $\delta_{F,3D}^{rec}$ of the three galaxy samples. The mean $\delta_{F,3D}^{rec}$ value of each sample is marked at the top axis.

redshift range are removed, we keep those without spectroscopic redshift. In all, we obtain 29 AGNs, of which seven do not have spectroscopic confirmation. Figure 8 shows the sky distribution of these AGNs overlaid on the LAE surface density map. These AGNs are preferentially found within the LAE overdensity or along the filamentary structures connected to them traced by LAEs and spectroscopic sources (Section 4.2).

There is a significant excess of AGNs in the protocluster region. Within our survey field, nine of the 17 X-ray AGNs lie inside the LAE overdensity, yielding the surface overdensity of $\delta_{\Sigma,X} = 7.8 \pm 3.4$. Similarly, nine of the 15 broad-line AGNs, three of the four MIPS-detected AGNs, and three of the eight radio AGNs reside within the $2.0\bar{\Sigma}$ isodensity contour or near it. When all types of AGNs are combined altogether, the AGN surface overdensity in Hyperion rises to $\delta_{\Sigma,\mathrm{all}} = 12.3 \pm 4.6$. For comparison, the LAE surface overdensity is $\delta_{\Sigma,\mathrm{LAE}} = 3.6 \pm 0.7$ (Section 4.1).

In these estimates, the errors represent Poisson fluctuations, which underestimate the true uncertainties for two reasons. First, these 29 AGNs are a subset of LAEs that already show a significant overdensity. Second, AGNs in general are known to be strongly clustered (e.g., Hickox et al. 2009) and thus are expected to have high cosmic variance. To evaluate the significance of the AGN excess in a more realistic manner, we create a mock AGN sample by randomly drawing 21 pLAEs and eight sLAEs from the respective samples, to match the makeup of the real AGN-LAEs. We then compute the inferred LAE overdensity of the mock sample. When repeated 10,000 times, we find that the LAE overdensity distribution is well described by a normal function with a mean $\mu = 2.63$ and a standard deviation $\sigma = 2.24$. The observed AGN overdensity, $\delta_{\Sigma,\mathrm{all}} = 12.3$, is 4.3σ away from the mean value. The likelihood of such an overdensity occurring from random fluctuations is $\approx 10^{-6}$.

The enhancement of AGN activity in dense environments has been reported by existing studies at high redshift. Lehmer et al. (2009) studied galaxies in the SSA22 protocluster, one of the best studied protocluster system at $z = 3.09$, and reported an enhancement of $4.9^{+11.7}_{-3.9}\%$ and $7.3^{+17.0}_{-6.2}\%$ in the X-ray-detected ($\log L_{8-32\,\mathrm{keV}} = 43.5-44.3$ erg s^{-1}) fraction in LBGs and LAEs, respectively. A similar trend was reported for lower-redshift protoclusters (Digby-North et al. 2010; Krishnan et al. 2017; Tozzi et al. 2022).

The prevalence of AGNs in protocluster cores or filaments is consistent with the scenario in which black hole activity is triggered due to the major mergers (Volonteri et al. 2003), which occur more frequently in a dense environment (e.g., Fakhouri & Ma 2009). The same scenario is supported by some

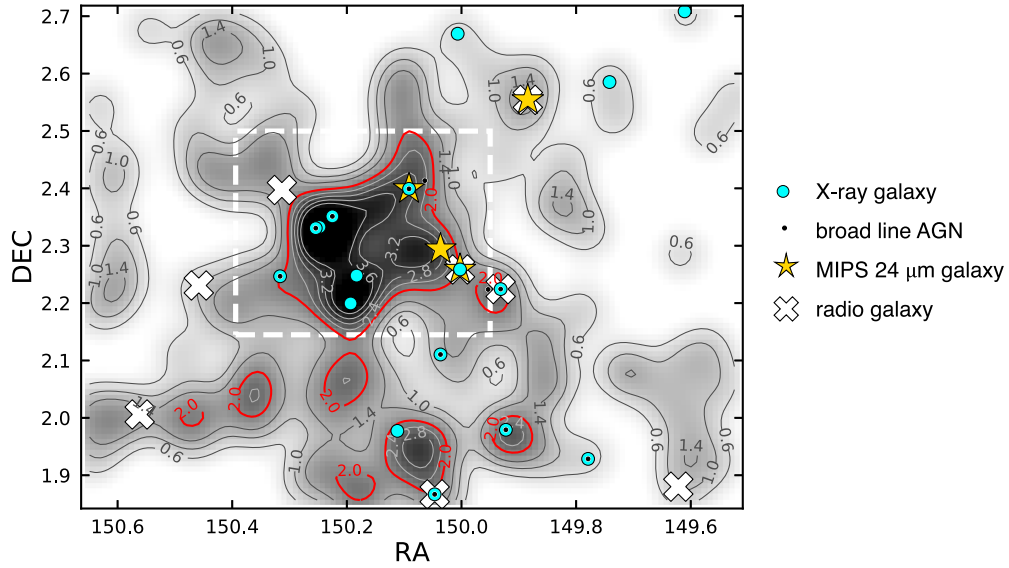

Figure 8. Sky positions of LAEs with X-ray (cyan circles), MIPS 24 μm (yellow stars), and VLA (white crosses) detection. The broad-line AGNs confirmed by spectroscopic surveys are shown as black dots. The smoothed LAE density map in the background and contours are identical to those shown in the top left panel of Figure 4.

observations: Hine et al. (2016) estimated the merger fraction of 0.48 ± 0.10 in the SSA22 protocluster relative to 0.33 ± 0.08 in the field. Similarly, Lotz et al. (2013) found a merger fraction of $0.57^{+0.13}_{-0.14}$ in a $z = 1.62$ protocluster, considerably higher than 0.11 ± 0.03 in the field. Whether a merger event is the dominant mechanism powering AGN activity is under debate. Shah et al. (2020) found a lack of enhancement in X-ray and IR-detected AGNs among mergers or close pairs, while Monson et al. (2021) reported that LBGs in the SSA22 protocluster exhibit similar merger rates as in the field.

Another phenomenon related to this may be extended LABs or "Lyα blobs." Several protoclusters show an excess number of blobs around galaxy overdensities (Matsuda et al. 2004; Prescott et al. 2008; Cai et al. 2017a; Badescu et al. 2017; Shi et al. 2019a). In SSA22, an overdensity of both AGNs (identified by X-ray and submillimeter observations; Umehata et al. 2019) and Lyα blobs (Matsuda et al. 2004) is found at the "nodes" of filaments traced by LAEs, hinting at the possible link between them. Indeed, AGNs are found in similar locations, close to the outskirts of dense cores (Shen et al. 2021) and filaments (Moutard et al. 2020). Like AGNs, the clustering strength of blobs indicates that they too are hosted by more massive halos than those hosting normal star-forming galaxies (e.g., Yang et al. 2010). Some blobs show direct evidence of being powered by AGNs (Overzier et al. 2013; Alexander et al. 2016; Cai et al. 2017b; Momose et al. 2019), while others point to cold gas accretion in dense environments (e.g., Daddi et al. 2021, 2022). These rare sources provide tantalizing evidence of processes uniquely occurring in protocluster environments.

Unfortunately, our current data are not equipped to identify blob candidates around Hyperion for the reasons described in Section 2.1. We are currently carrying out deeper observations of several fields including COSMOS to identify the candidates (B. Moon et al., in preparation, V. Ramakrishnan, in preparation). Considering the relatively short duty cycle expected for these phenomena, the most robust constraints on the physical connection between protoclusters, AGNs, and blobs will require a large-area blind survey that can discover a statistical sample of protoclusters (see Section 5.2).

5. Discussion

5.1. Intrinsic Galaxy Overdensity of Hyperion

The NB422 filter has a width 170 Å and samples 170 cMpc in the line-of-sight distance at $z \approx 2.4$. This is much greater than the size of a typical protocluster,; thus we expect that the spatial overdensity, δ_g, of the structure is greater than the measured surface overdensity, which is diluted by unassociated fore- and background sources. Here, we estimate the true overdensity of the structure traced by our LAEs.

First, we create a field with a mock protocluster positioned at its center. The protocluster region is defined as a rectangle whose area is equal to that enclosed by the $2.0\bar{\Sigma}$ isodensity contour[19] outlined in red in the left panel of Figure 4. In the line-of-sight direction, the observed survey range [2.40, 2.54] is divided into 11 bins with an interval $\Delta z = 0.013$, corresponding to 15 cMpc, roughly matching the half-mass diameter of a massive protocluster (Chiang et al. 2013; Muldrew et al. 2015). In this setup, the true number of galaxies in a protocluster would be $N_{\rm pc} = (1 + \delta_g)N_{\rm obs}/(N_z + \delta_g)$, where $N_{\rm obs}$ is the total number of LAEs found in the protocluster region, δ_g is the galaxy overdensity in the redshift space, $N_z = 11$ is the number of bins within the observed survey range, and $N_{\rm obs} = 40$ is the total LAEs detected in the protocluster region. Then we randomly choose a δ_g value in the range 0–50, compute the number of protocluster and field galaxies (including their Poisson shot noise), and populate them in the 3D space. The surface overdensity δ_Σ is computed from the run, yielding the δ_g–δ_Σ scaling relation given our observational parameters. The procedure is repeated 10,000 times.

The recovered δ_g–δ_Σ is linear and well-behaved. The LAE surface overdensity $\delta_\Sigma = 3.7$ implies $\delta_g = 39.6^{+5.4}_{-5.1}$, much higher than the $\delta_g \sim 3$–10 expected for a single protocluster (e.g., Cucciati et al. 2014; Lemaux et al. 2014; Topping et al. 2018;

[19] The transverse size is 18×12 arcmin^2 or 30×20 cMpc^2 at $z = 2.4$.

Shi et al. 2019b; Hu et al. 2021). The unphysically high galaxy overdensity is a direct result of our simplistic assumption that there is a *single* protocluster, which is easily disputed by the redshift distribution of our LAEs (Section 4.2).

We repeat the procedure, but this time assuming four protoclusters. For the lack of better information about the relative size of the structures within Hyperion and their configuration, we assume that each protocluster is confined in a rectangular region 6′ on a side (10.2 cMpc at $z = 2.4$) with the identical overdensity. We obtain $\delta_g = 12.2^{+2.8}_{-2.0}$. Similarly, assuming seven protoclusters in the region as was found by Cucciati et al. (2018), each structure is expected to have $\delta_g = 5.9$–8.3. While simplistic, our analysis demonstrates that the significance and the angular extent of the LAE overdensity is too great for a single protocluster but instead requires at least three massive overlapping ones, reinforcing the notion that LAEs provide an effective pathway to find cosmic structures or a complex of structures in distant universe.

Using these δ_g estimates for each protocluster, we can make a crude estimate of the total mass locked in them. The main limitation comes from our lack of knowledge about the relative sizes of individual groups and their configuration; additionally, if a substantial fraction of LAEs trace the filaments connecting the main halos, it would lead to an overestimation of the total mass.

Following the method outlined in Steidel et al. (1998), the descendant mass of a structure is expressed as

$$M_{\rm tot} = \bar{\rho} V_{\rm true} (1 + \delta_m), \tag{4}$$

where $\bar{\rho}$ is the mean density of the universe and $V_{\rm true}$ is the true volume that encloses the structure. The matter overdensity, δ_m, is related to galaxy overdensity as $1 + b\delta_m = C(1 + \delta_g)$, where $C \equiv V_{\rm obs}/V_{\rm true}$ is a correction factor for redshift space distortion arising from peculiar velocities. In the case of spherical collapse, $C = 1 + \Omega_m^{4/7}(z)[1 - (1 + \delta_m)^{1/3}]$. For $V_{\rm obs}$, we assume the line-of-sight distance 15 cMpc. We adopt a galaxy bias parameter $b = 2$ for LAEs (Gawiser et al. 2007; Guaita et al. 2010). The total mass enclosed therein is $M_{\rm tot} = 1.4^{+0.2}_{-0.1} \times 10^{15}\ M_\odot$. The bias value of $b = 2.5$ would decrease the mass by 14% to $1.2 \times 10^{15}\ M_\odot$. Our estimate of the total mass within this volume does not depend on the assumed number of protoclusters.

When compared with existing measurements, our estimate should be considered with caution. First, it is larger by a factor of 2 than the sum total of the seven Hyperion density peaks, $\approx 4.8 \times 10^{14}\ M_\odot$, estimated by Cucciati et al. (2018). This is expected because our estimate includes not only the masses of the individual protoclusters but also the filaments and walls between them. Second, our estimate is ≈ 3 times smaller than the total mass of Hyperion, $\approx 4.8 \times 10^{15}\ M_\odot$, estimated by the same authors. As illustrated in the top left panel of Figure 5, what is considered as the spatial extent of Hyperion (black dashed line) is substantially larger than the LAE overdensity in the transverse direction and possibly in the z direction as well. For the benefit of future protocluster studies, perhaps what is more useful is to test how reliably the present-day mass of a single cosmic structure can be derived through spectroscopy and/or LAE overdensity. To that end, a similar analysis of relatively isolated protoclusters is needed.

5.2. Future Outlook: LAEs as Beacons of Protoclusters

The present study unambiguously demonstrates LAEs as reliable markers of the largest cosmic structures such as protoclusters and groups of protoclusters. Further, their distribution can be used to estimate the size, morphology, and present-day mass of the structure and to reveal regions of interest such as dense cores, filaments, and voids. These capabilities will be valuable in any systematic effort to study cosmic structures that lie outside a handful of deep extragalactic fields with extensive spectroscopy.

The One-hundred-square-degree DECam Imaging in Narrowbands (ODIN) survey has been conducting deep imaging of $\approx 100\ {\rm deg}^2$ in area using the Dark Energy Camera (Flaugher et al. 2015) to identify LAEs, LABs, and forming protoclusters. ODIN targets three cosmic epochs at $z = 4.5$, 3.1, and 2.4, straddling the crucial epoch in which the mass assembly in field and cluster galaxies reached its peak (e.g., Madau & Dickinson 2014; Chiang et al. 2017). Over seven fields,[20] ODIN will sample a total of $\approx 0.25\ {\rm Gpc}^3$ in cosmic volume in which $\approx$130,000 LAEs and $\approx$45 (600) progenitors of Coma- and Virgo-like clusters ($M_{\rm tot} > 10^{15}\ M_\odot$and $(3$–$10) \times 10^{14}\ M_\odot$, respectively) are expected. The details of the survey will be presented in an upcoming paper (K.-S. Lee et al. 2022, in preparation).

When combined with the new generation of wide-field imaging and spectroscopic experiments such as LSST, Roman, LMT/TolTEC, HETDEX, and DESI, ODIN will open up a new window into the formation of cosmic structures and the role of large-scale environment on the galaxy constituents therein. First, the physical connection between protoclusters, AGNs, LABs, and passive galaxies can be quantified and delineated in a statistically meaningful manner. Measurements of their occurrences, preferred locations, and physical properties can be used to place strong constraints on the physical origin and the timescale of these phenomena.

Second, a robust sample of protoclusters with accurate redshifts will facilitate comparative studies. Recently, large samples of protocluster candidates have been identified as LBG overdensities (e.g., Toshikawa et al. 2016, 2018) and cold dust emission in the far-IR (e.g., Planck Collaboration et al. 2015, 2016). However, the intersection between these samples and the selection efficiency and bias of different techniques are poorly understood (but see, e.g., Negrello et al. 2017; Gouin et al. 2022).

Finally, a large statistical sample of ODIN protoclusters will allow us to measure the average star formation activity expected in a protocluster and how it scales with their present-day masses over cosmic time. For example, deep wide-field millimeter surveys such as the LMT/TolTEC Public Legacy survey will not only detect individual high star formers but can also be used to estimate the total (dust-obscured) SFR per cluster via stacking analysis. Such measurements can resolve or further highlight the current tension that exists between the observed and predicted level of star formation in protoclusters (e.g., Lim et al. 2021).

6. Summary

In this paper, we carry out a comprehensive study of galaxies inhabiting Hyperion, the first spectroscopically confirmed

[20] The targeted fields include all four LSST Deep Drilling Fields, two southern Euclid Deep fields, Deep2-3, and HETDEX-SHELA.

structure that hosts multiple protoclusters at $z = 2.4$–2.5, which will likely evolve into a supercluster of galaxies by the present-day universe. To trace its large-scale structure (LSS), we obtain deep narrowband observations of $\approx 1^\circ \times 1^\circ$ of the region using NB422 ($\lambda_c \approx 4225$ Å, $\Delta\lambda = 170$ Å) and select 157 LAE candidates at the Hyperion redshift (Section 3.1). The new data combined with the extensive spectroscopic and photometric observations available in the field provide a unique opportunity to closely examine how galaxies of different types trace the same large-scale structure. Our main findings are listed below:

1. A significant excess of LAEs occupies the region of Hyperion with a surface overdensity $\delta_\Sigma = 3.6$ (Section 4.1). This corresponds to the combined spatial galaxy overdensity $\delta_g \approx 40$ within an effective volume of $30 \times 20 \times 15$ cMpc^3. The level and the extent of the overdensity is too large for a single structure, strongly suggesting that multiple protoclusters must be embedded in Hyperion. The LAE overdensity will evolve into a supercluster of galaxies with a total mass of $M_{\rm tot} \approx 1.4 \times 10^{15}\ M_\odot$ distributed between the main halos hosting each protocluster and the filaments connecting them (Section 5.1).
2. Taking advantage of the densely sampled spectroscopic data, we evaluate the feasibility of LAEs as a probe of the LSS in and around Hyperion (Section 4.2). The distributions of LAEs and spectroscopic sources are remarkably similar, suggesting that LAEs are excellent tracers of the LSS (Figure 5). In particular, the LAE distribution clearly marks several density peaks and extended structures in Hyperion. However, we also find tentative evidence that LAEs may be poor tracers of the most evolved systems (e.g., see Wang et al. 2016).
3. Using the COSMOS2015 and COSMOS2020 photometric redshift catalogs, we construct a local density map at $z = 2.40$–2.54. The photoz map fares reasonably well in finding several strongest features of Hyperion, including the highest galaxy overdensities and the lowest-density voids around it. However, lower-density features of interest such as filaments are better traced by line-emitting galaxies (Figure 6).
4. By cross-correlating the LAE positions with the H I tomography data from the CLAMATO survey (Lee et al. 2016), we find that LAEs tend to lie in the regions of moderate H I overdensities while avoiding the highest H I density regions (Figure 7). Our finding is in line with existing studies (e.g., Momose et al. 2021) and is consistent with the expectation that the suppression of Lyα transmission may be substantial in the highest-density regions due to resonant scattering.
5. In and around Hyperion, we find a significant overdensity of AGNs (Section 4.5, Figure 8) selected based on X-ray/radio/mid-IR emission or broad emission line features including Lyα. When all types of AGNs are considered together, the surface overdensity is measured to be $\delta_{\Sigma,all} \approx 12$, that is, 3.5 times larger than the LAE surface overdensity of the region, $\delta_{\Sigma,\rm LAE} = 3.6$. The prevalence of AGNs in protocluster regions hints at the possibility that they may be triggered by physical processes that occur more frequently in dense environments, such as galaxy mergers.

The authors acknowledge financial support from NASA through the Astrophysics Data Analysis Program, grant No. 80NSSC19K0582, and from the Ross-Lynn PRF Research Grant, id. 60000031. The observation is based on observations at Kitt Peak National Observatory, NSF's National Optical-Infrared Astronomy Research Laboratory (NOIRLab Prop. ID: 2018A-0446, 2018B-0376, 2019A-0372, 2019B-0483; PI: K.-S. Lee), which is operated by the Association of Universities for Research in Astronomy (AURA) under a cooperative agreement with the National Science Foundation. The *u*-band data were obtained and processed as part of the CFHT Large Area *U*-band Deep Survey (CLAUDS), which is a collaboration between astronomers from Canada, France, and China described in Sawicki et al. (2019, [MNRAS 489, 5202]). CLAUDS is based on observations obtained with MegaPrime/MegaCam, a joint project of CFHT and CEA/DAPNIA, at the CFHT, which is operated by the National Research Council (NRC) of Canada, the Institut National des Science de l'Univers of the Centre National de la Recherche Scientifique (CNRS) of France, and the University of Hawaii. CLAUDS uses data obtained in part through the Telescope Access Program (TAP), which has been funded by the National Astronomical Observatories, the Chinese Academy of Sciences, and the Special Fund for Astronomy from the Ministry of Finance of China. CLAUDS uses data products from TERAPIX and the Canadian Astronomy Data Centre (CADC) and was carried out using resources from Compute Canada and Canadian Advanced Network For Astrophysical Research (CANFAR). Some of the material presented in this paper is based upon work supported by the National Science Foundation under grant No. 1908422. B.C.L. acknowledges support from the National Science Foundation under grant No. 1908422.

ORCID iDs

Yun Huang https://orcid.org/0000-0002-2073-5325
Kyoung-Soo Lee https://orcid.org/0000-0003-3004-9596
Olga Cucciati https://orcid.org/0000-0002-9336-7551
Brian C. Lemaux https://orcid.org/0000-0002-1428-7036
Marcin Sawicki https://orcid.org/0000-0002-7712-7857
Nicola Malavasi https://orcid.org/0000-0001-9033-7958
Rui Xue https://orcid.org/0000-0001-7689-9305
Letizia P. Cassara https://orcid.org/0000-0001-5760-089X
Yi-Kuan Chiang https://orcid.org/0000-0001-6320-261X
Arjun Dey https://orcid.org/0000-0002-4928-4003
Stephen D. J. Gwyn https://orcid.org/0000-0001-8221-8406
Nimish Hathi https://orcid.org/0000-0001-6145-5090
Laura Pentericci https://orcid.org/0000-0001-8940-6768
Moire K. M. Prescott https://orcid.org/0000-0001-8302-0565
Gianni Zamorani https://orcid.org/0000-0002-2318-301X

References

Adams, J. J., Blanc, G. A., Hill, G. J., et al. 2011, ApJS, 192, 5
Adelberger, K. L., Steidel, C. C., Shapley, A. E., & Pettini, M. 2003, ApJ, 584, 45
Aihara, H., AlSayyad, Y., Ando, M., et al. 2019, PASJ, 71, 114
Alberts, S., Pope, A., Brodwin, M., et al. 2016, ApJ, 825, 72
Alexander, D. M., Simpson, J. M., Harrison, C. M., et al. 2016, MNRAS, 461, 2944
Badescu, T., Yang, Y., Bertoldi, F., et al. 2017, ApJ, 845, 172
Beckmann, R. S., Devriendt, J., Slyz, A., et al. 2017, MNRAS, 472, 949
Bertin, E., & Arnouts, S. 1996, A&AS, 117, 393

Bertin, E., Mellier, Y., Radovich, M., et al. 2002, in ASP Conf. Ser. 281, The TERAPIX Pipeline, ed. D. A. Bohlender, D. Durand, & T. H. Handley (San Francisco, CA: ASP), 228
Blandford, R. D., & Payne, D. G. 1982, MNRAS, 199, 883
Bridle, A. H., & Perley, R. A. 1984, ARA&A, 22, 319
Cai, Z., Fan, X., Bian, F., et al. 2017a, ApJ, 839, 131
Cai, Z., Fan, X., Yang, Y., et al. 2017b, ApJ, 837, 71
Casey, C. M., Cooray, A., Capak, P., et al. 2015, ApJL, 808, L33
Chiang, Y.-K., Overzier, R., & Gebhardt, K. 2013, ApJ, 779, 127
Chiang, Y.-K., Overzier, R., & Gebhardt, K. 2014, ApJL, 782, L3
Chiang, Y.-K., Overzier, R. A., Gebhardt, K., et al. 2015, ApJ, 808, 37
Chiang, Y.-K., Overzier, R. A., Gebhardt, K., & Henriques, B. 2017, ApJL, 844, L23
Chiappetti, L., Tajer, M., Trinchieri, G., et al. 2005, A&A, 439, 413
Ciardullo, R., Gronwall, C., Adams, J. J., et al. 2013, ApJ, 769, 83
Civano, F., Marchesi, S., Comastri, A., et al. 2016, ApJ, 819, 62
Cooke, E. A., Hatch, N. A., Muldrew, S. I., Rigby, E. E., & Kurk, J. D. 2014, MNRAS, 440, 3262
Cooper, M. C., Newman, J. A., Weiner, B. J., et al. 2008, MNRAS, 383, 1058
Coppin, K., Pope, A., Menendez-Delmestre, K., et al. 2010, ApJ, 713, 503
Cucciati, O., Lemaux, B. C., Zamorani, G., et al. 2018, A&A, 619, A49
Cucciati, O., Zamorani, G., Lemaux, B. C., et al. 2014, A&A, 570, A16
Daddi, E., Rich, R. M., Valentino, F., et al. 2022, ApJL, 926, L21
Daddi, E., Valentino, F., Rich, R. M., et al. 2021, A&A, 649, A78
Dey, A., Lee, K.-S., Reddy, N., et al. 2016, ApJ, 823, 11
Diener, C., Lilly, S. J., Ledoux, C., et al. 2015, ApJ, 802, 31
Digby-North, J. A., Nandra, K., Laird, E. S., et al. 2010, MNRAS, 407, 846
Eisenhardt, P. R. M., Brodwin, M., Gonzalez, A. H., et al. 2008, ApJ, 684, 905
Fakhouri, O., & Ma, C.-P. 2009, MNRAS, 394, 1825
Faucher-Giguere, C.-A., Prochaska, J. X., Lidz, A., Hernquist, L., & Zaldarriaga, M. 2008, ApJ, 681, 831
Flaugher, B., Diehl, H. T., Honscheid, K., et al. 2015, AJ, 150, 150
Gaia Collaboration, Prusti, T., de Bruijne, J. H. J., et al. 2016, A&A, 595, A1
Gawiser, E., Francke, H., Lai, K., et al. 2007, ApJ, 671, 278
Gawiser, E., van Dokkum, P. G., Gronwall, C., et al. 2006, ApJL, 642, L13
Gisler, G. R. 1978, MNRAS, 183, 633
Gopu, A., Hayashi, S., Young, M. D., et al. 2014, Proc. SPIE, 9152, 91520E
Gouin, C., Aghanim, N., Dole, H., Polletta, M., & Park, C. 2022, A&A, 664, A155
Gronwall, C., Ciardullo, R., Hickey, T., et al. 2007, ApJ, 667, 79
Guaita, L., Acquaviva, V., Padilla, N., et al. 2011, ApJ, 733, 114
Guaita, L., Gawiser, E., Padilla, N., et al. 2010, ApJ, 714, 255
Harbeck, D. R., Boroson, T., Lesser, M., et al. 2014, Proc. SPIE, 9147, 91470P
Harbeck, D. R., Lesser, M., Liu, W., et al. 2018, Proc. SPIE, 10702, 1070229
Harikane, Y., Ouchi, M., Ono, Y., et al. 2019, ApJ, 883, 142
Hatch, N. A., Kurk, J. D., Pentericci, L., et al. 2011, MNRAS, 415, 2993
Hayashi, M., Kodama, T., Tadaki, K.-i., Koyama, Y., & Tanaka, I. 2012, ApJ, 757, 15
Hayashino, T., Matsuda, Y., Tamura, H., et al. 2004, AJ, 128, 2073
Hennawi, J. F., Prochaska, J. X., Cantalupo, S., & Arrigoni-Battaia, F. 2015, Sci, 348, 779
Hickox, R. C., Jones, C., Forman, W. R., et al. 2009, ApJ, 696, 891
Hine, N. K., Geach, J. E., Alexander, D. M., et al. 2016, MNRAS, 455, 2363
Hopkins, P. F., Keres, D., Onorbe, J., et al. 2014, MNRAS, 445, 581
Hu, W., Wang, J., Infante, L., et al. 2021, NatAs, 5, 485
Intema, H. T., Venemans, B. P., Kurk, J. D., et al. 2006, A&A, 456, 433
Kashikawa, N., Kitayama, T., Doi, M., et al. 2007, ApJ, 663, 765
Komiyama, Y., Obuchi, Y., Nakaya, H., et al. 2018, PASJ, 70, S2
Koyama, Y., Smail, I., Kurk, J., et al. 2013, MNRAS, 434, 423
Krishnan, C., Hatch, N. A., Almaini, O., et al. 2017, MNRAS, 470, 2170
Kurk, J. D., Pentericci, L., Rottgering, H. J. A., & Miley, G. K. 2004, A&A, 428, 793
Kusakabe, H., Shimasaku, K., Ouchi, M., et al. 2018, PASJ, 70, 4
Laigle, C., McCracken, H. J., Ilbert, O., et al. 2016, ApJS, 224, 24
Le Fevre, O., Tasca, L. A. M., Cassata, P., et al. 2015, A&A, 576, A79
Lee, K.-G., Hennawi, J. F., Stark, C., et al. 2014a, ApJL, 795, L12
Lee, K.-G., Hennawi, J. F., White, M., et al. 2016, ApJ, 817, 160
Lee, K.-S., Dey, A., Hong, S., et al. 2014b, ApJ, 796, 126
Lehmer, B. D., Alexander, D. M., Geach, J. E., et al. 2009, ApJ, 691, 687
Lemaux, B. C., Cucciati, O., Tasca, L. A. M., et al. 2014, A&A, 572, A41
Lemaux, B. C., Cucciati, O., Le Fèvre, O., et al. 2022, A&A, 662, A33
Lilly, S. J., Fevre, O. L., Renzini, A., et al. 2007, ApJS, 172, 70
Lilly, S. J., Le Brun, V., Maier, C., et al. 2009, ApJS, 184, 218
Lim, S., Scott, D., Babul, A., et al. 2021, MNRAS, 501, 1803
Lotz, J. M., Papovich, C., Faber, S. M., et al. 2013, ApJ, 773, 154
Madau, P., & Dickinson, M. 2014, ARA&A, 52, 415
Marchesi, S., Civano, F., Elvis, M., et al. 2016, ApJ, 817, 34
Martin-Navarro, I., Vazdekis, A., Falcon-Barroso, J., et al. 2018, MNRAS, 475, 3700
Matsuda, Y., Yamada, T., Hayashino, T., et al. 2004, AJ, 128, 569
Matsuda, Y., Yamada, T., Hayashino, T., et al. 2005, ApJL, 634, L125
McConachie, I., Wilson, G., Forrest, B., et al. 2022, ApJ, 926, 37
Miyazaki, S., Komiyama, Y., Kawanomoto, S., et al. 2018, PASJ, 70, S1
Mo, W., Gonzalez, A., Stern, D., et al. 2018, ApJ, 869, 131
Momose, R., Goto, T., Utsumi, Y., et al. 2019, MNRAS, 488, 120
Momose, R., Shimasaku, K., Kashikawa, N., et al. 2021, ApJ, 909, 117
Monson, E. B., Lehmer, B. D., Doore, K., et al. 2021, ApJ, 919, 51
Moutard, T., Malavasi, N., Sawicki, M., Arnouts, S., & Tripathi, S. 2020, MNRAS, 495, 4237
Muldrew, S. I., Hatch, N. A., & Cooke, E. A. 2015, MNRAS, 452, 2528
Nakajima, K., Ouchi, M., Shimasaku, K., et al. 2012, ApJ, 745, 12
Negrello, M., Gonzalez-Nuevo, J., De Zotti, G., et al. 2017, MNRAS, 470, 2253
Newman, A. B., Rudie, G. C., Blanc, G. A., et al. 2020, ApJ, 891, 147
Oke, J. B., & Gunn, J. E. 1983, ApJ, 266, 713
Ouchi, M., Ono, Y., & Shibuya, T. 2020, ARA&A, 58, 617
Ouchi, M., Shimasaku, K., Akiyama, M., et al. 2008, ApJS, 176, 301
Overzier, R. A. 2016, A&ARv, 24, 14
Overzier, R. A., Bouwens, R. J., Illingworth, G. D., & Franx, M. 2006, ApJL, 648, L5
Overzier, R. A., Nesvadba, N. P. H., Dijkstra, M., et al. 2013, ApJ, 771, 89
Penny, S. J., Masters, K. L., Smethurst, R., et al. 2018, MNRAS, 476, 979
Planck Collaboration, Ade, P. A. R., Aghanim, N., et al. 2014, A&A, 571, A28
Planck Collaboration, Ade, P. A. R., Aghanim, N., et al. 2016, A&A, 596, A100
Planck Collaboration, Aghanim, N., Altieri, B., et al. 2015, A&A, 582, A30
Prescott, M. K. M., Kashikawa, N., Dey, A., & Matsuda, Y. 2008, ApJL, 678, L77
Sanders, D. B., Salvato, M., Aussel, H., et al. 2007, ApJS, 172, 86
Sawicki, M., Arnouts, S., Huang, J., et al. 2019, MNRAS, 489, 5202
Schinnerer, E., Sargent, M. T., Bondi, M., et al. 2010, ApJS, 188, 384
Shah, E. A., Kartaltepe, J. S., Magagnoli, C. T., et al. 2020, ApJ, 904, 107
Shen, L., Lemaux, B. C., Lubin, L. M., et al. 2021, ApJ, 912, 60
Shi, K., Huang, Y., Lee, K.-S., et al. 2019a, ApJ, 879, 9
Shi, K., Lee, K.-S., Dey, A., et al. 2019b, ApJ, 871, 83
Shimakawa, R., Kodama, T., Tadaki, K.-i., et al. 2014, MNRAS, 441, L1
Shimakawa, R., Kodama, T., Hayashi, M., et al. 2018, MNRAS, 473, 1977
Snyder, G. F., Brodwin, M., Mancone, C. M., et al. 2012, ApJ, 756, 114
Somerville, R. S., & Dave, R. 2015, ARA&A, 53, 51
Stanford, S. A., Eisenhardt, P. R., & Dickinson, M. 1998, ApJ, 492, 461
Steidel, C. C., Adelberger, K. L., Dickinson, M., et al. 1998, ApJ, 492, 428
Stevens, J. A., Jarvis, M. J., Coppin, K. E. K., et al. 2010, MNRAS, 405, 2623
Topping, M. W., Shapley, A. E., Steidel, C. C., Naoz, S., & Primack, J. R. 2018, ApJ, 852, 134
Toshikawa, J., Kashikawa, N., Ota, K., et al. 2012, ApJ, 750, 137
Toshikawa, J., Kashikawa, N., Overzier, R., et al. 2016, ApJ, 826, 114
Toshikawa, J., Uchiyama, H., Kashikawa, N., et al. 2018, PASJ, 70, S12
Tozzi, P., Pentericci, L., Gilli, R., et al. 2022, A&A, 662, A54
Trainor, R. F., & Steidel, C. C. 2012, ApJ, 752, 39
Umehata, H., Fumagalli, M., Smail, I., et al. 2019, Sci, 366, 97
Vanden Berk, D. E., Richards, G. T., Bauer, A., et al. 2001, AJ, 122, 549
Venemans, B. P., Kurk, J. D., Miley, G. K., et al. 2002, ApJL, 569, L11
Venemans, B. P., Rottgering, H. J. A., Miley, G. K., et al. 2007, A&A, 461, 823
Volonteri, M., Haardt, F., & Madau, P. 2003, ApJ, 582, 559
von der Linden, A., Wild, V., Kauffmann, G., White, S. D. M., & Weinmann, S. 2010, MNRAS, 404, 1231
Wang, T., Elbaz, D., Daddi, E., et al. 2016, ApJ, 828, 56
Weaver, J. R., Kauffmann, O. B., Ilbert, O., et al. 2022, ApJS, 258, 11
Wold, M., Armus, L., Neugebauer, G., Jarrett, T. H., & Lehnert, M. D. 2003, AJ, 126, 1776
Yang, Y., Zabludoff, A., Eisenstein, D., & Dave, R. 2010, ApJ, 719, 1654
Yang, Y., Zabludoff, A., Tremonti, C., Eisenstein, D., & Dave, R. 2009, ApJ, 693, 1579
Zheng, X. Z., Cai, Z., An, F. X., Fan, X., & Shi, D. D. 2021, MNRAS, 500, 4354